Supporting Information

High Interfacial Charge Storage Capability of Carbonaceous Cathodes for Mg Batteries

Lu Wang,[†] Bo Jiang,[†] Per Erik Vullum,[‡,§] Ann Mari Svensson,[†] Andreas Erbe,[†] Sverre M. Selbach,[†] Huailiang Xu,[∥] and Fride Vullum-Bruer*[†]

[†]Department of Materials Science and Engineering, Norwegian University of Science and Technology, NO-7491 Trondheim, Norway

[‡]SINTEF Materials and Chemistry, NO-7491 Trondheim, Norway

[§]Department of Physics, Norwegian University of Science and Technology, NO-7491 Trondheim, Norway

[∥]The Sixth Element (Changzhou) Materials Technology Co., Ltd., 213000 Changzhou, China

*Corresponding Authors. E-mail: fride.vullum-bruer@ntnu.no

Table of Contents

Part 1. Chemical System of APC Electrolyte

The standard APC electrolyte is synthesized by an in-situ reaction between a Lewis acid ($AlCl_3$) and a Lewis base (PhMgCl), and involves transmetalation in which the chloride ligands and solvent molecules reside primarily on the Mg core, and the phenyl groups are preferentially bound to Al. The reaction formula is shown below:

$$9PhMgCl + 4.5AlCl_3 \rightarrow Ph_4Al^- + 2Ph_2AlCl_2^- + PhAlCl_3^- + 0.5AlCl_4^- + 4.5Mg_2Cl_3^+$$

This kind of transmetalation reaction leads to coexistence of various Al species with the $Mg_2Cl_3^+$ dimer as the major Mg species under dynamic equilibria in the *esol*.[1] All the species in this mixture are coordinated by solvent molecules, and the electrochemical characteristics of the APC electrolyte are determined by the complexity of its composition. Normally, with the combination of phenyl groups, chloride or *esol* molecules, Al keeps a coordination number of four, while Mg always maintains a coordination number of six.[2] The *esol*s here act as a strong donor and have a dramatic effect on the complex cation formation. The major Mg complex in the bulk of a typical APC electrolyte (with THF as solvent) is proven to be the Mg dimer $[Mg_2(\mu\text{-}Cl)_3 \cdot 6THF]^+$.[3-5] At the electrode/electrolyte interface, the Mg dimers decompose to form Mg monomers, $[MgCl \cdot 5THF]^+$, which strongly adsorb on the surface of the electrode and are the active Mg species for charge transfer across the interface.[5,6]

Part 2. Materials Characterizations

Elemental analysis

Elemental analyses of graphite, GiO and MEGO were performed, and the results are shown in Table S1. The dramatic increase in oxygen content from ~0 wt% in the graphite sample to 45.87 wt% in GiO confirms the successful oxidation of graphite. In the final product, MEGO, the oxygen content is reduced to approximately 5 wt% with a C/O ratio of about 18.

Table S1. Elemental analysis, specific surface area and electronic conductivity of Graphite, GiO and MEGO

Materials	C (wt%)	O (wt%)	H (wt%)	N (wt%)	C/O	BET ($m^2 g^{-1}$)	Conductivity ($S\ m^{-1}$)
Graphite	99.2	0.01	-	-	-	29.7	$4.02 \cdot 10^2$
GiO	48.9	45.9	2.26	0.09	1.07	70.4	$1.21 \cdot 10^{-5}$
MEGO	91.4	5.05	0.85	0.18	18.1	144	$0.81 \cdot 10^2$

FTIR analysis

The results from ATR-FTIR spectroscopy in Figure S1a support the oxygen decrease from GiO to MEGO. The GiO spectrum illustrates the characteristic features including broad stretching vibration peak of O-H groups (carboxylic) centred around 3400 cm^{-1}, the C=O stretching vibration peak (carbonyl and carboxyl) at 1723 cm^{-1}, the C-O-C (epoxy) stretching vibration peak at 1200 cm^{-1}, and the C-O (alkoxy) stretching vibration peak at 1028 cm^{-1}. The peak

around 1580 cm^{-1} is assigned to the vibrations of the intercalated water molecules and also somewhat contributes from the C=C skeletal vibrations of non-oxidized graphitic domains.[7-10] In the spectra for graphite and MEGO, these peaks are virtually gone.

TGA analysis

The oxygen content of the three graphitic materials was also verified by TGA. Figure S1b shows that the mass of the graphite and MEGO samples are nearly constant upon heating to 800 °C, while the mass loss for GiO is close to 50%. The mass loss observed for the GiO powders occurs in two stages. The mass loss below 150 °C corresponds to the elimination of interlamellar water, while the major mass loss from 150 °C to approximately 200 °C is caused by pyrolysis of the labile oxygen groups, generating CO and CO_2.[11-13] This material also continues to lose mass upon further heating, which can be attributed to further reduction of the GiO and loss of the remaining surface groups.

XRD analysis

In Figure S1c the position of the (002) peak of graphite is $2\theta = 26.6°$, which corresponds to an interlayer distance of ~3.34 Å. Whereas GiO displays a broad peak near 12.4° with a *d*-spacing of 7.13 Å as a consequence of insertion of a substantial amount of oxygen-groups into the graphitic interlayers, indicating the complete transformation from graphite to GiO.[14,15] MEGO also displays a peak at 26.6°, but the intensity is negligible compared with that observed for graphite and GiO. This is an indication of the disordered structure of MEGO and substantial deoxygenation from GiO to MEGO.[14]

Raman analysis

Further structural information can be extracted from the Raman spectra in Figure S1d. The G band of GiO (1600 cm^{-1}) is broadened and up-shifted compared with that of graphite (1581 cm^{-1}), which mainly owning to the presence of isolated double bonds that resonate at frequencies higher than that of graphite.[16,17] The approach in peak position of G-band between MEGO (1587 cm^{-1}) and graphite states the recovery hexagonal carbon network.[18] Moreover, the higher I_D/I_G ratio for MEGO (1.27) than for GiO (0.89) implies a decrease in size of the sp^2 domains and an alteration of the structure of GiO with a high quantity of structural defects appearing upon thermal reduction from GiO to MEGO.[12,19]
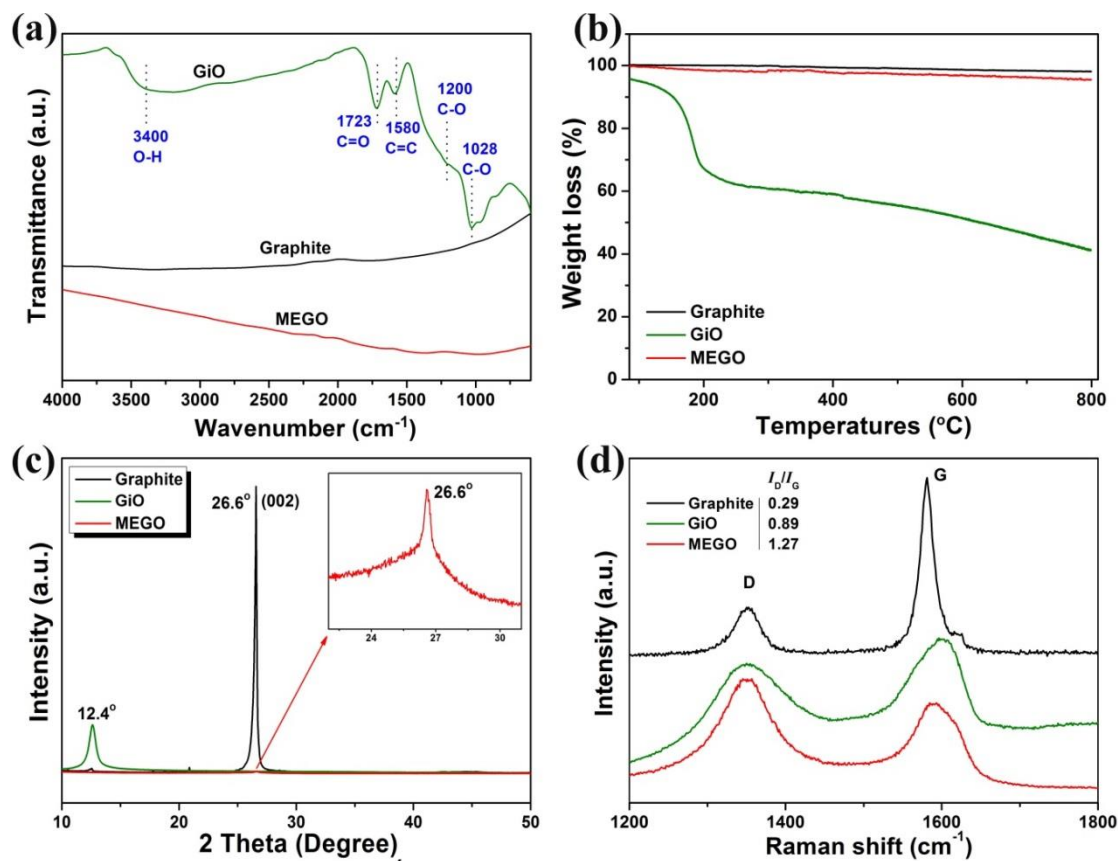
Figure S1. (a) ATR-FTIR spectra, (b) TGA thermograms, (c) XRD patterns and (d) Raman spectra of graphite, GiO and MEGO. Inset: the magnified region of the XRD pattern of MEGO.

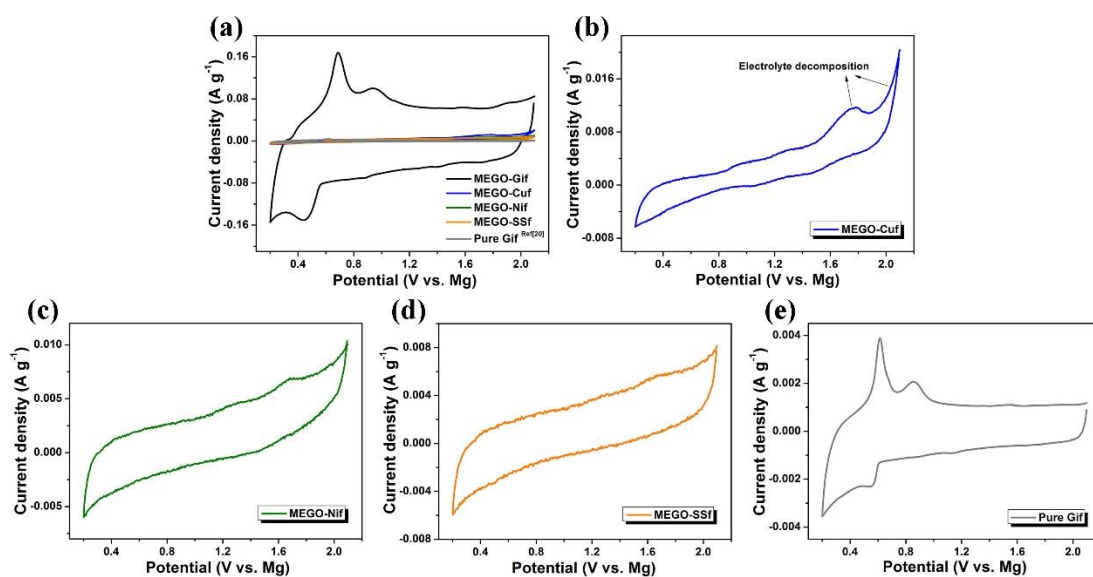## Part 3. CV Curves of MEGO Electrodes on Different Current Collectors

Figure S2. (a) Comparison of CV curves at 0.2 mV s^{-1} in APC-THF electrolyte. CV curves of (b) MEGO-Cuf, (c) MEGO-Nif, (d) MEGO-SSf and (e) pure Gif (which is referred from our previous work, Ref [20]) at 0.2 mV s^{-1} in APC-THF electrolyte.

Figure S2 shows some obvious redox peaks in the region between about 0.4 and 1.0 V for MEGO on Gif, while essentially no peaks are visible when Ni (Nif), Cu (Cuf) or stainless steel (SSf) are used as current collectors. This may be caused by the high contact resistance between the electrode and metallic current collectors according to the inclined CV curves of the MEGO cathodes on metallic current collectors. Compared with the metallic current collectors, Gif provides much better adherence between the current collector and the electrode materials, allowing the interfacial reactions to easily proceed. Additionally, as shown in Figure S2a and S2e, the negligible capacity measured for the pure Gif (~0.5 mAh g^{-1} at 20 mA g^{-1})[20] does in fact show that the high reversible capacities of the MEGO cathode in APC-THF electrolyte (see Figure 2e) originate from the MEGO nanosheets, and not from the Gif current collector.

Part 4. Analysis of Mg Plating/Stripping on the Surface of Pt or Gif

In Figure S3, two distinct peaks appear in the CV curves of both Gif and Pt as working electrode (WE), one cathodic peak and one anodic peak, corresponding to Mg plating and stripping, respectively. In addition, for the Gif electrode, there are other reactions occurring as well during Mg plating/stripping, as shown in Figure S3b. A relatively low current can be observed at positive potentials, corresponding to the dark grey area in Figure S3b. This cannot be due to Mg plating and must therefore be caused by some unknown reactions. The blue area corresponds mainly to Mg stripping. During Mg stripping there also seems to be an unknown contribution above about 0.8 V, which is indicated by the light grey part of the CV curve during oxidation. The different electrochemical behaviour of Gif and Pt in APC electrolyte may be due to the different adsorption properties of the Mg cations on these two working electrodes. There is chemical bonding between the chlorinated surface of Pt and the $MgCl^+$ complex, while only weak Van der Waals interactions exist between the chlorinated surface of graphite and the $MgCl^+$ complex (see the following detailed analysis), which results in the physical plating/stripping of Mg cations on the Gif surface. This weak interaction between graphite and the Mg cations will likely lead to partial desolvation of the Mg complexes at the electrode/electrolyte interface during cycling, and thus provide enhanced capacity.
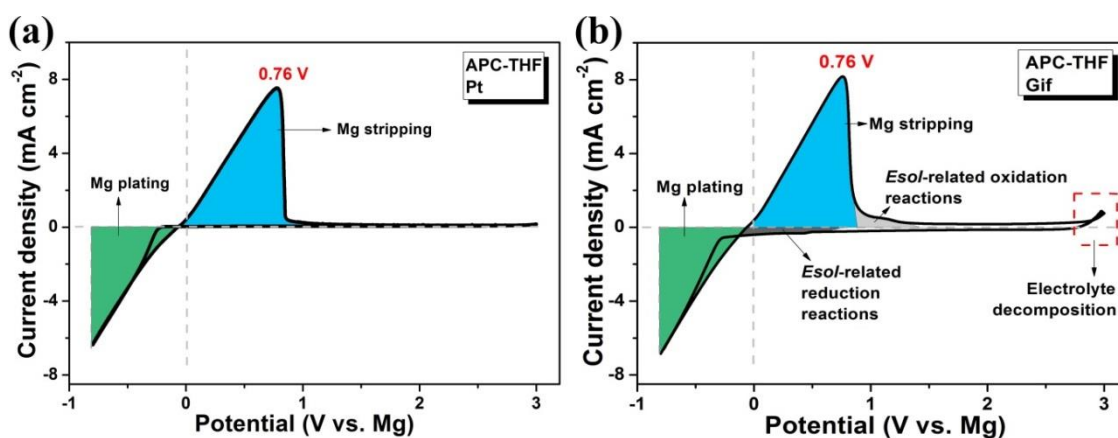

Figure S3. Typical CV curves of Mg plating/stripping in 0.4 M APC-THF electrolyte. Experiments are carried out on Pt (a) and Gif (b), at 10 mV s^{-1} with Mg metal as both reference- and counter electrode.

Computational details:

The standard PBE PAW potentials C ($2s^2 2p^2$), Pt ($4d^{10}$), Mg_pv ($2p^6 3s^2$) and Cl ($3s^2 3p^5$) potentials supplied with Vienna Ab initio Simulation Package (VASP) VASP were used for slab calculations using the PBEsol functional. Brillouin zone integration was done on a $2\times2\times1$ k-point grid with a cut off energy of 500 eV for the slab surface calculations, and the forces on the ions were relaxed until they were below 0.01 eV $Å^{-1}$. The adsorption slabs were cleaved from the relaxed Pt and graphite bulk structure. The working electrode surfaces comprised of graphite(001), Pt(001), Pt(011) and Pt(111) with expansion in the a and b directions from the primitive cell. All the slabs have at least four-layers periodic structure with a 20 Å vacuum. For all slab models, ionic positions in the top two layers were optimized, while the structure volume and shape were kept fixed. Dipole corrections[21] were used to avoid asymmetric slab error to the total energy introduced by the periodic boundary conditions. The adsorption sites investigated were top, bridge and hollow sites. All the calculations were performed with VASPsol and the solvent dielectric constant was set to 7.58 in order to simulate THF solvation effects.

Weak long-range van der Waals (vdW)[22] interactions were also taken into account for the graphite system. The vdW calculations were carried out self-consistently using an implementation of Grimme's DFT-D2 approach in VASP.

Interfacial adsorption energies (ΔE) for working electrode (WE, which is Pt or graphite) were calculated using the equations below:

$$\Delta E(Cl^-/WE) = E_o(WE + Cl^-) - E_o(WE) - E_o(Cl^-) \qquad (S1)$$

$$\Delta E(Mg^{2+}/WE) = E_o(WE + Mg^{2+}) - E_o(WE) - E_o(Mg^{2+}) \qquad (S2)$$

$$\Delta E(MgCl_2/WE) = E_o(WE + MgCl_2) - E_o(MgCl_2) \qquad (S3)$$

where $E_o(WE + M)$ (M= Cl^-, Mg^{2+} and $MgCl_2$) is the total energy of the WE's surface and the adsorbing species. $E_o(WE)$ is the energy of the slab surface. $E_o(Mg^{2+})$, $E_o(Cl^-)$ and $E_o(MgCl^+)$ are the energies of the Mg^{2+}, Cl^- and $MgCl^+$, respectively, which are calculated in a large non-cubic unit cell of a size $11\times10\times9$ Å to break initial symmetry.

Discussion:

Based on the recent studies of Ceder *et al.*[6] and Gewirth *et al.*[23,24], Mg plating is achieved with the assistance of Cl^- adsorbed on the surface of the working electrode (WE). The free Cl^- ions in APC electrolyte first chlorinate the WE's surface, resulting in the formation of the enhancement layer, which might benefit the transfer of electrons to the electrolyte species.[24] In order to study the different Mg plating/stripping behaviours on Pt and Gif, we calculated the interaction energies of Cl^- + $MgCl^+$ adsorption on different surface sites of Pt and graphite by using Equations (S1-3). From the results shown in Table S2, the Cl^- ions are more likely to be adsorbed on the bridge sites of Pt(001) and Pt(011), and on the hollow site of Pt(111), while Mg^{2+} cations prefer to absorb on the hollow sites of Pt(001), Pt(011) and Pt(111). Through the interaction of $MgCl^+$ with the Cl^- ions on the surface of Pt, Mg cations strongly adsorb on the

surface of Pt (see Table S2 and Figure S5a-5c), facilitating the following Mg plating. In the case of graphite, the strong interaction of Cl^- ions with the graphite(001) (see Table S2) indicates that the surface of graphite will be chlorinated by the free Cl^- ions in APC electrolyte prior to Mg plating. However, there are weak van der Waals interactions between Mg^{2+} cations and both chlorinated graphite and unchlorinated graphite (see Table S2), and physical adsorption of metal on graphite (or graphene) has been reported in other studies.[25-28] Therefore, the nature of Mg plating varies with different WEs, with chemical Mg plating observed on the Pt surface and physical Mg plating on the graphite surface.
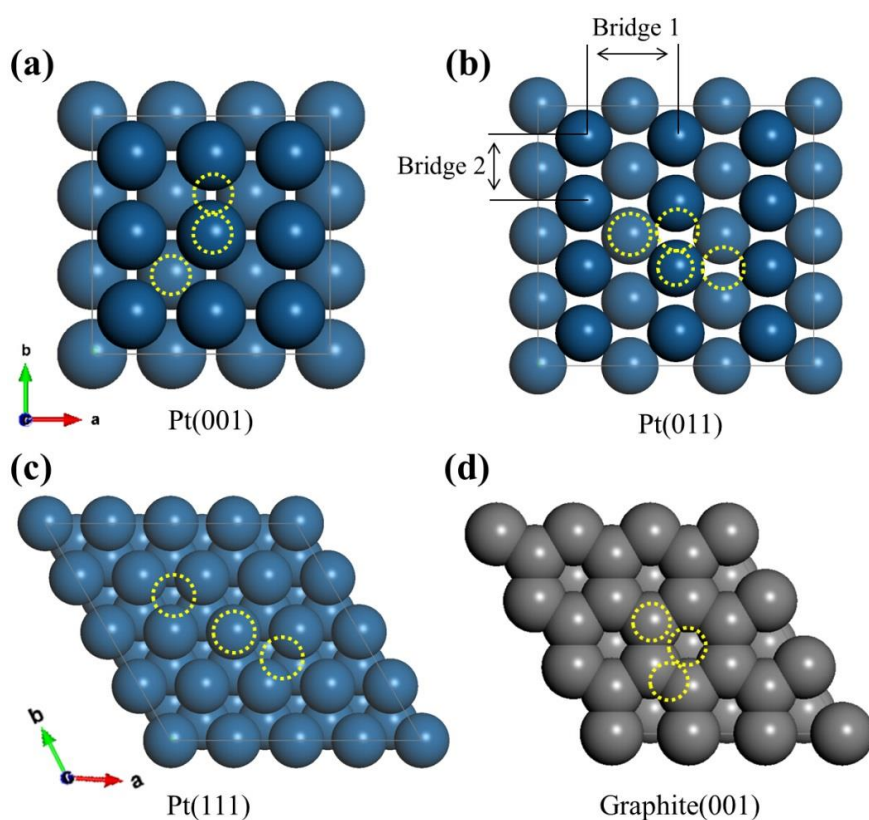

Figure S4. Slab models of (a) Pt(001), (b) Pt(011), (c) Pt(111) and (d) graphite(001) surfaces and the selected top, bridge, hollow adsorption sites (marked with yellow dash line). Lower surface coverages (1/9 ML, 1/12 ML, 1/16 ML, 1/18 ML, respectively) were performed in this work.
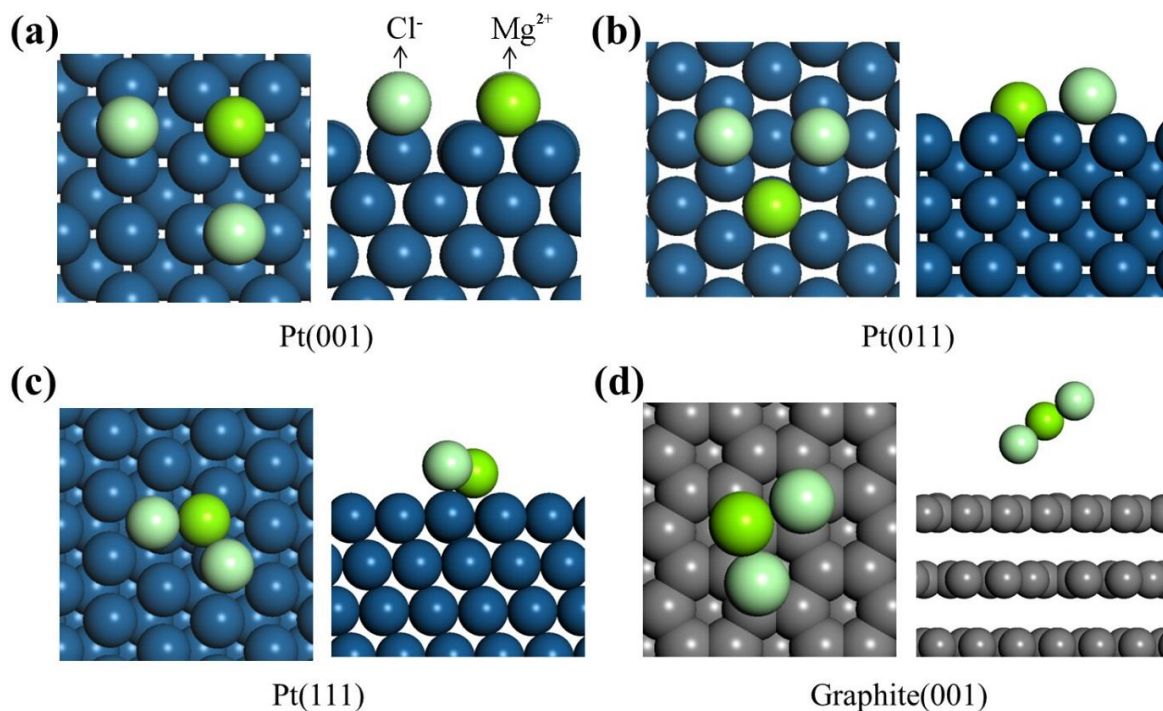
Figure S5. MgCl₂ adsorption and interaction on (a) Pt(001), (b) Pt(011), (c) Pt(111) and (d) graphite(001) surfaces.

Table S2. The calculated interaction energies (eV) of Cl⁻ + MgCl⁺ adsorption on different Pt and graphite surface sites

Surface	Site	$\Delta E(Cl^-/WE)$	$\Delta E(Mg^{2+}/WE)$	$\Delta E(MgCl_2/WE)$	$R_{pt\text{-}Cl}$/Å	$R_{pt\text{-}Mg}$/Å
Pt(001)	top	-2.88	-3.94		2.24	2.40
	bridge	-3.54	-4.37	-1.97	2.31	2.55
	hollow	-3.23	-4.87		2.52	2.70
Pt(011)	top	-3.34	-4.42		2.25	2.49
	bridge 1	-3.54	-4.75		2.36	2.62
	bridge 2	-3.68	-4.62	-2.42	2.34	2.63
	hollow	-2.85	-4.89		2.71	2.84
Pt(111)	top	-2.76	-4.43		2.26	2.47
	bridge	-3.06	-4.71	-1.19	2.36	2.62
	hollow	-3.27	-4.75		2.40	2.71
Graphite (001)	top	-1.21	-0.07		2.64	3.05
	bridge	-1.18	-0.06	-0.04	2.83	3.10
	hollow	-1.14	-0.06		3.24	3.13

Part 5. Kinetics and Quantitative Analyses Method

Kinetics Analysis

Assuming that the response current (i), which can stem from the diffusion-controlled reactions or/and the non-diffusion controlled contribution, as a function of scan rate (v) obeys a power-law relationship: $i = av^b$ or $\log i = \log a + b \log v$,[29] where a and b are adjustable parameters. A linear plot of log i vs. log v gives the b-value as the slope of the linear regression. A b-value of 1 is expected for the non-diffusion controlled processes and occur at the outer and easily accessible active surfaces.[30-34] While a b-value of 0.5 is expected for the diffusion-controlled reactions and processes occurring at the inner or less-easily accessible surfaces, which are usually limited by the slow kinetics of ion diffusion.[31,34,35]

Quantitative Analysis

The contributions from both the diffusion-controlled reactions and capacitive processes can be qualitatively quantified by separating the response current at a fixed potential (V) into diffusion controlled reactions ($k_2v^{1/2}$) and surface-controlled capacitive processes (k_1v) by using $i(V) = k_1v + k_2v^{1/2}$.[31,36] The fraction of these two contributions can be quantified by determining both the k_1 and k_2 constants through the slope of the linear plot of $v^{1/2}$ vs $i\, v^{-1/2}$.[31]

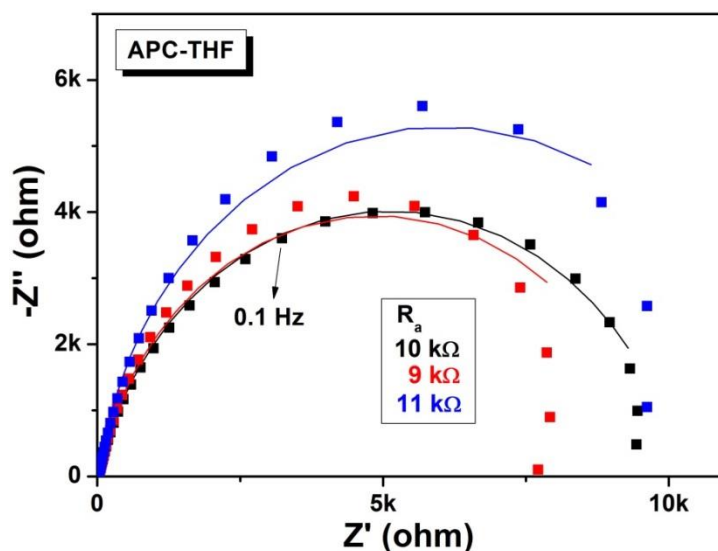## Part 6. Nyquist Plots of MEGO Electrodes in APC-THF Electrolyte

Figure S6. The Nyquist plots of MEGO electrodes at different cell states (fresh (black), first discharge (red) and second discharge (blue)) in APC-THF electrolyte under the frequency range of 10^4 Hz to 0.01 Hz. Note that the high R_a values were measured at open circuit voltage (OCV), and they may decrease during cycling.

Part 7. Ex-situ XRD Characterizations of MEGO Electrodes in Different APC Electrolytes
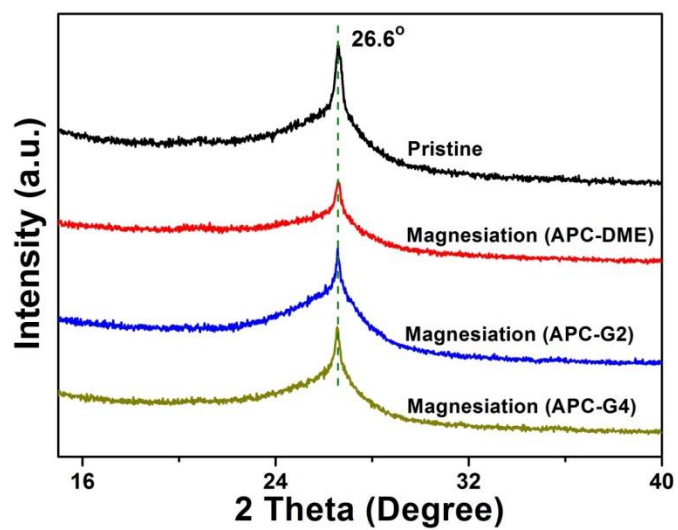

Figure S7. Ex-situ XRD patterns of MEGO electrodes after magnesiation under 10 mA g^{-1} in APC electrolytes with chain-type *esol*s.

Part 8. Kinetics and Quantitative Analyses of MEGO Electrodes in Different APC Electrolytes
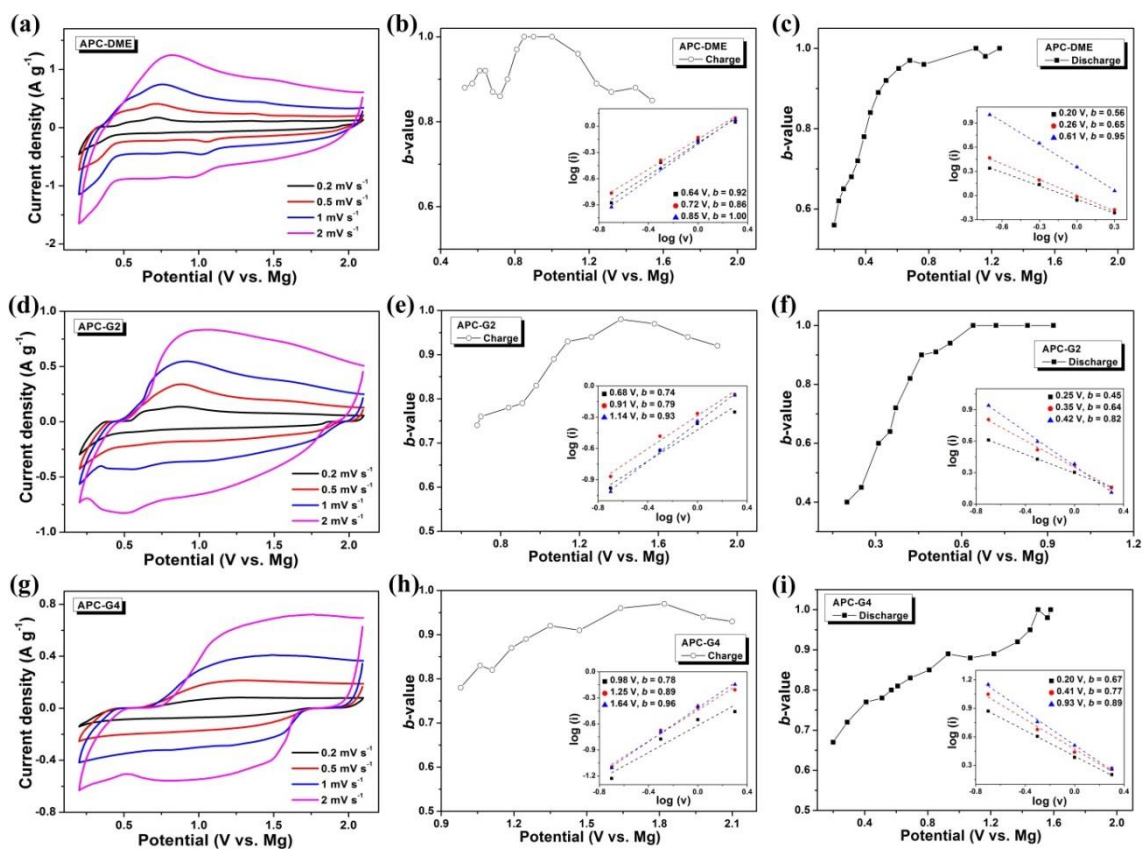

Figure S8. (a,d,g) CV curves of MEGO at varying scan rates in APC electrolytes with chain-typed *esol*s. (b,c,e,f,h,i) Dependence of *b*-values as a function of potential. Insets: power law dependence of current on scan rate.
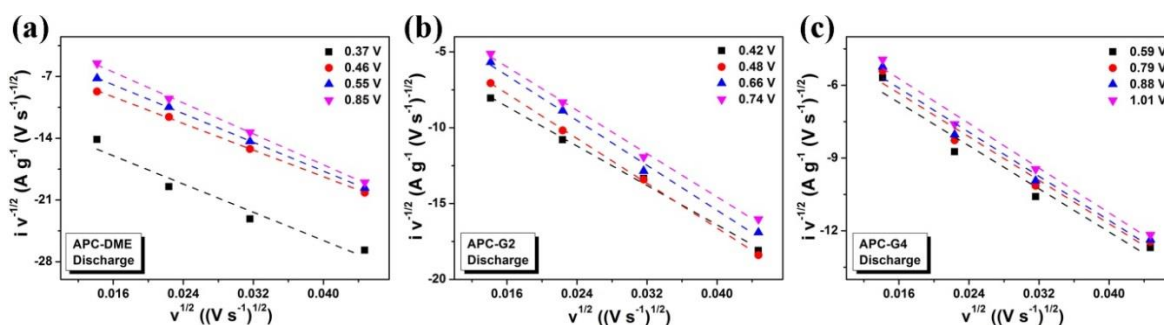

Figure S9. Plots of $v^{1/2}$ vs $i\ v^{-1/2}$, v varies from 0.2 to 2 mV s^{-1}.

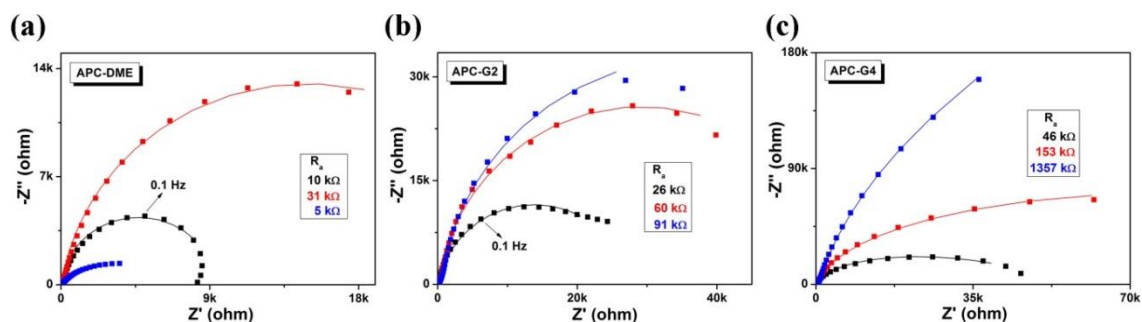## Part 9. Nyquist Plots of MEGO Electrodes in Different APC Electrolytes

Figure S10. The Nyquist plots of MEGO electrodes at different cell states (fresh (black), first discharge (red) and second discharge (blue)) in (a) APC-DME, (b) APC-G2 and (c) APC-G4 electrolytes under the frequency range of 10^4 Hz to 0.01 Hz. Note that the high R_a values were measured at OCV, and they may decrease during cycling.

Part 10. Ex-situ ATR-FTIR Characterization of MEGO Electrodes in APC-DME Electrolyte

Figure S11 shows the ex-situ IR spectra acquired in inert atmosphere (Ar), of charged and discharged electrodes. Although this data is not conclusive with regards to the charge storage mechanism, it provides further insight into the differences between charged and discharged surfaces. Electrodes were sealed off against ingress from air during the transfer into the spectrometer.

The non-baseline corrected ATR-IR spectra of the pristine MEGO electrode shows the typical strong absorption without features, as expected for a conductive material. In the charged state, the background absorption from free carriers is also present, with dominating peaks in the region of 1000-1100 cm^{-1}. In this region, strong backbone modes from organic molecules are typically found, especially with heteroatoms such as oxygen.[37] Vibrational modes indicating the presence of C-H or C=O groups are absent. (The differences in the baseline absorption compared to MEGO may be due to differences in amount of sample analyzed.) Consequently, spectra are in agreement with the formation of C-O-C structures on the MEGO surface.

In the discharged state, the baseline is flat, indicating that no free carrier absorption takes place in the area in contact with the ATR crystal. Thus, a layer with a thickness above the penetration depth of an evanescent wave, i.e. on the order of ~500 nm was formed, which is essentially free of carbonaceous species. Instead, the layer contains molecular organic species. Spectra contain C-H stretching modes both above and below 3000 cm^{-1}, indicating the presence of both aliphatic as well as unsaturated hydrocarbons.[37] Peaks of carbonyl groups, expected in the region between 1550-1750 cm^{-1},[37] are absent. Likewise, the typical features from the aromatic ring stretching modes observed around 1500 and 1600 cm^{-1} are absent. In combination with the observation of C-H stretching modes from unsaturated hydrocarbons, this indicates the presence of C=C double bonds. The associated absorption feature is typically very weak, due

to its low transition dipole moment. Dominating features of the spectra are observed at 1097, 1059 and 1038 cm^{-1}, the latter with a shoulder around 1030 cm^{-1}. The spectra of pure DME, as well as DME complexes with bivalent cations such as Ca^{2+} and Sr^{2+} show their main absorption features above 1100 cm^{-1}.[38]

On the other hand, spectra of the polymeric Mg^{2+} complex-$[Mg(\mu-Cl)_2(DME)]_n$ reported by Pakkanen *et al.*[39] show a number of similar features as observed in the spectra in this work. There is a significant change of the spectrum of DME in such a complex. It is therefore concluded that in the discharged state, a redox process may be triggering some interfacial changes that lead to the formation of the polymeric Mg^{2+} complex with solvent coordination.

Spectra in the charged state still show the baseline absorption from the MEGO substrate, indicating that the thickness of a formed surface layer is significantly smaller than the penetration depth of the evanescent wave, at best 10s of nm. Some spectral features agree with those observed in the discharged state, however, overall, the spectra are substantially different. The dominating vibrational feature around 1040 cm^{-1} is also in line with the interpretation that C-O bonds are contained in the adsorbed surface species.

Consequently, changes near the electrode environment triggered during charging are likely to lead to a polymeric complex containing DME. The charging process in part must involve a reversible decomposition of this polymeric complex. On the other hand, the purely capacitive component of the charge storage mechanism is hard to probe by ex situ techniques, as the electrode relaxes during the withdrawal from the electrolyte.
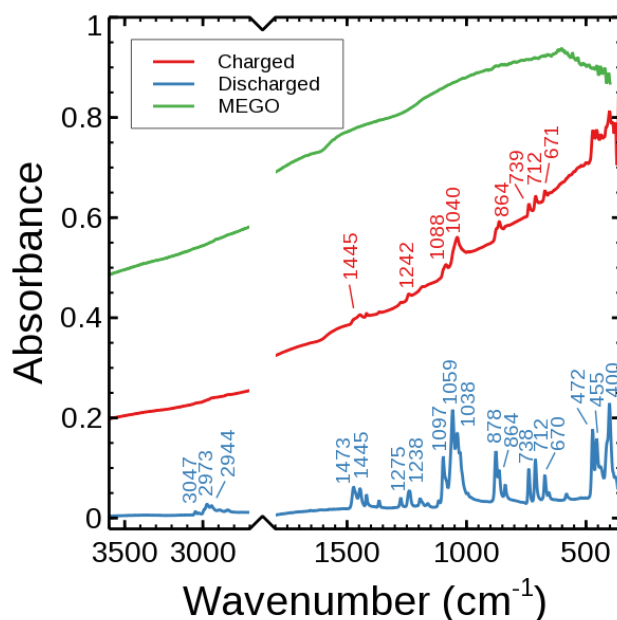

Figure S11. Ex-situ ATR-FTIR spectra acquired in Ar atmosphere of MEGO electrodes at different cell stages in APC-DME electrolyte. For comparison, the spectrum of pristine MEGO is also included. No baseline treatment was performed.

Part 11. Analysis of Stability of Mg Dimers with Different *Esol*s

The interaction energies $\Delta E(Mg_2Cl_3^+/esol)$ of $Mg_2Cl_3^+$ with the *esol* have been calculated by using the following equation:

$$\Delta E(Mg_2Cl_3^+/esol) = E_o(Mg_2Cl_3^+ + esol) - E_o(Mg_2Cl_3^+) - 6E_0(esol)$$

where $E_o(Mg_2Cl_3^+ + esol)$ is the total energy of the $Mg_2Cl_3^+$ with six *esol* molecules, $E_o(Mg_2Cl_3^+)$ is the energy of the $Mg_2Cl_3^+$ in a large unit cell of $10\times10\times10$Å and $E_0(esol)$ is the energy of a single solvent molecule in a unit cell of $20\times20\times20$Å.

Table S3. The calculated interaction energies (eV) between $Mg_2Cl_3^+$ and the coordinated *esol* molecules for solvent system

	$Mg_2Cl_3^+ + 6THF$	$Mg_2Cl_3^+$	THF	ΔE
Energy (eV)	-456.25	-14.08	-72.99	-4.24
	$Mg_2Cl_3^+ + 6DME$	$Mg_2Cl_3^+$	DME	
Energy (eV)	-535.94	-13.98	-86.72	-1.57
	$Mg_2Cl_3^+ + 6G2$	$Mg_2Cl_3^+$	G2	
Energy (eV)	-775.25	-13.99	-126.62	-1.56
	$Mg_2Cl_3^+ + 6G4$	$Mg_2Cl_3^+$	G4	
Energy (eV)	-1253.39	-14.14	-206.37	-1.01

Part 12. References

(1) Pour, N.; Gofer, Y.; Major, D. T.; Aurbach, D. Structural Analysis of Electrolyte Solutions for Rechargeable Mg Batteries by Stereoscopic Means and DFT Calculations. *J. Am. Chem. Soc.* **2011**, *133*, 6270-6278.

(2) Yoo, H. D.; Shterenberg, I.; Gofer, Y.; Gershinsky, G.; Pour, N.; Aurbach, D. Mg Rechargeable Batteries: An on-Going Challenge. *Energy Environ. Sci.* **2013**, *6*, 2265-2279.

(3) Muldoon, J.; Bucur, C. B.; Oliver, A. G.; Sugimoto, T.; Matsui, M.; Kim, H. S.; Allred, G. D.; Zajicek, J.; Kotani, Y. Electrolyte Roadblocks to a Magnesium Rechargeable Battery. *Energy Environ. Sci.* **2012**, *5*, 5941-5950.

(4) Bucur, C. B.; Gregory, T.; Oliver, A. G.; Muldoon, J. Confession of a Magnesium Battery. *J. Phys. Chem. Lett.* **2015**, *6*, 3578-3591.

(5) Benmayza, A.; Ramanathan, M.; Arthur, T. S.; Matsui, M.; Mizuno, F.; Guo, J.; Glans, P. A.; Prakash, J. Effect of Electrolytic Properties of a Magnesium Organohaloaluminate Electrolyte on Magnesium Deposition. *J. Phys. Chem. C* **2013**, *117*, 26881-26888.

(6) Canepa, P.; Gautam, G. S.; Malik, R.; Jayaraman, S.; Rong, Z.; Zavadil, K. R.; Persson, K.; Ceder, G. Understanding the Initial Stages of Reversible Mg Deposition and Stripping in Inorganic Nonaqueous Electrolytes. *Chem. Mater.* **2015**, *27*, 3317-3325.

(7) Guo, H.; Wang, X.; Wang, F.; Qian, Q.; Xia, X. A Green Approach to the Synthesis of Graphene Nanosheets. *ACS Nano* **2009**, *3*, 2653-2659.

(8) Zhang, J.; Yang, H.; Shen, G.; Cheng, P.; Zhang, J.; Guo, S. Reduction of Graphene Oxide via L-Ascorbic Acid. *Chem. Commun.* **2010**, *46*, 1112-1114.

(9) Lin, Z.; Yao, Y.; Li, Z.; Liu, Y.; Li, Z.; Wong, C. P. Wrinkled Graphenes: A Study on the Effects of Synthesis Parameters on Exfoliation-Reduction of Graphite Oxide. *J. Phys. Chem. C* **2011**, *115*, 17660-17669.

(10) Xu, Y.; Bai, H.; Lu, G.; Li, C.; Shi, G. Flexible Graphene Films via the Filtration of Water-Soluble Noncovalent Functionalized Graphene Sheets. *J. Am. Chem. Soc.* **2008**, *130*, 5856-5857.

(11) Stankovich, S.; Dikin, D. A.; Piner, R. D.; Kohlhaas, K. A.; Kleinhammes, A.; Jia, Y.; Wu, Y.; Nguyen, S. T.; Ruoff, R. S. Synthesis of Graphene-Based Nanosheets Via Chemical Reduction of Exfoliated Graphite Oxide. *Carbon* **2007**, *45,* 1558-1565.

(12) Choi, E. Y.; Han, T. H.; Hong, J. H.; Kim, J. E.; Lee, S. H.; Kim, H. W.; Kim, S. O. Noncovalent Functionalization of Graphene with End-Functional Polymers. *J. Mater. Chem.* **2010**, *20,* 1907-1912.

(13) Lerf, A.; He, H. Y.; Forster, M.; Klinowski, J. Structure of Graphite Oxide Revisited. *J. Phys. Chem. B* **1998**, *102,* 4477-4482.

(14) Xie, J.; Li, C.; Cui, Z.; Guo, X. Transition-Metal-Free Magnesium-Based Batteries Activated by Anionic Insertion into Fluorinated Graphene Nanosheets. *Adv. Funct. Mater.* **2015**, *25,* 6519-6526.

(15) Chen, C. M.; Yang, Q. H.; Yang, Y. G.; Lv, W.; Wen, Y. F.; Hou, P. X.; Wang, M. Z.; Cheng, H. M. Self-Assembled Free-Standing Graphite Oxide Membrane. *Adv. Mater.* **2009**, *21,* 3007-3011.

(16) Ferrari, A. C.; Robertson, J. Interpretation of Raman Spectra of Disordered and Amorphous Carbon. *Phys. Rev. B* **2000**, *61*, 14095-14107.

(17) Moon, I. K.; Lee, J.; Ruoff, R. S.; Lee, H. Reduced Graphene Oxide by Chemical Graphitization. *Nat. Comm.* **2010**, *1*, 73-78.

(18) Wang, Z. F.; Wang, J. Q.; Li, Z. P.; Gong, P. W.; Liu, X. H.; Zhang, L. B.; Ren, J. F.; Wang, H. G.; Yang, S. R. Synthesis of Fluorinated Graphene with Tunable Degree of Fluorination. *Carbon* **2012**, *50*, 5403-5410.

(19) Tuinstra, F.; Koenig, J. L. Raman Spectrum of Graphite. *J. Chem. Phys.* **1970**, *53,* 1126.

(20) Wang, L.; Asheim, K.; Vullum, P. E.; Svensson, A. M.; Vullum-Bruer, F. Sponge-Like Porous Manganese(II,III) Oxide as a Highly Efficient Cathode Material for Rechargeable Magnesium Ion Batteries. *Chem. Mater.* **2016**, *28*, 6459-6470.

(21) Neugebauer, J.; Scheffler, M. Adsorbate-Substrate and Adsorbate-Adsorbate Interactions of Na and K Adlayers on Al(111). *Phys. Rev. B* **1992**, *46*, 16067-16080.

(22) Dion, M.; Rydberg, H.; Schroder, E.; Langreth, D. C.; Lundqvist, B. I. Van der Waals Density Functional for General Geometries. *Phys. Rev. Lett.* **2004**, *92*, 246401.

(23) See, K. A.; Chapman, K. W.; Zhu, L.; Wiaderek, K. M.; Borkiewicz, O. J.; Barile, C. J.; Chupas, P. J.; Gewirth, A. A. The Interplay of Al and Mg Speciation in Advanced Mg Battery Electrolyte Solutions. *J. Am. Chem. Soc.* **2016**, *138*, 328-337.

(24) Esbenshade, J. L.; Barile, C. J.; Fister, T. T.; Bassett, K. L.; Fenter, P.; Nuzzo, R. G.; Gewirth, A. A. Improving Electrodeposition of Mg through an Open Circuit Potential Hold. *J. Phys. Chem. C* **2015**, *119*, 23366-23372.

(25) Appy, D.; Lei, H.; Wang, C. Z.; Tringides, M. C.; Liu, D. J.; Evans, J. W.; Thiel, P. A. Transition Metals on the (0 0 0 1) Surface of Graphite: Fundamental Aspects of Adsorption, Diffusion, and Morphology. *Prog. Surf. Sci.* **2014**, *89*, 219-238.

(26) Tachikawa, H.; Iyama, T.; Kawabata, H. MD Simulation of the Interaction of Magnesium with Graphene. *Thin Solid Films* **2009**, *518*, 877-879.

(27) Förster, G. D.; Rabilloud, F.; Calvo, F. Adsorption of Metal Nanoparticles on Carbon Substrates and Epitaxial Graphene: Assessing Models for Dispersion Forces. *Phys. Rev. B* **2015**, *91*, 245433.

(28) Mellita, C.; Sharon, F. *J. Phys.: Condens. Matter* **2005**, *17*, R995-R1024.

(29) Lindstrom, H.; Sodergren, S.; Solbrand, A.; Rensmo, H.; Hjelm, J.; Hagfeldt, A.; Lindquist, S. E. Li^+ Ion Insertion in TiO_2 (Anatase). 2. Voltammetry on Nanoporous Films. *J. Phys. Chem. B* **1997**, *101,* 7717-7722.

(30) Augustyn, V.; Simon, P.; Dunn, B. Pseudocapacitive Oxide Materials for High-Rate Electrochemical Energy Storage. *Energy Environ. Sci.* **2014**, *7,* 1597-1614.

(31) Wang, J.; Polleux, J.; Lim, J.; Dunn, B. Pseudocapacitive Contributions to Electrochemical Energy Storage in TiO_2 (Anatase) Nanoparticles. *J. Phys. Chem. C* **2007**, *111,* 14925-14931.

(32) Augustyn, V.; Come, J.; Lowe, M. A.; Kim, J. W.; Taberna, P. L.; Tolbert, S. H.; Abruna, H. D.; Simon, P.; Dunn, B. High-Rate Electrochemical Energy Storage through Li^+ Intercalation Pseudocapacitance. *Nat. Mater.* **2013**, *12,* 518-522.

(33) Simon, P.; Gogotsi, Y.; Dunn, B. Where Do Batteries End and Supercapacitors Begin? *Science* **2014**, *343,* 1210-1211.

(34) Sathiya, M.; Prakash, A. S.; Ramesha, K.; Tarascon, J. M.; Shukla, A. K. V_2O_5-Anchored Carbon Nanotubes for Enhanced Electrochemical Energy Storage. *J. Am. Chem. Soc.* **2011**, *133,* 16291-16299.

(35) Ardizzone, S.; Fregonara, G.; Trasatti, S. Inner and Outer Active Surface of RuO_2 Electrodes. *Electrochim. Acta* **1990**, *35,* 263-267.

(36) Chao, D.; Zhu, C.; Yang, P.; Xia, X.; Liu, J.; Wang, J.; Fan, X.; Savilov, S. V.; Lin, J.; Fan, H. J.; Shen, Z. X. Array of Nanosheets Render Ultrafast and High-Capacity Na-Ion Storage by Tunable Pseudocapacitance. *Nat. Commun.* **2016**, *7,* 12122.

(37) Nyquist, R. A. Interpreting Infrared, Raman, and Nuclear Magnetic Resonance Spectra; Academic Press: San Diego, **2001**; Vol 1.

(38) Fukushima, K.; Chibahara, H. Conformational Difference Due to Types of Cation in 1,2 Dimethoxyethane-Cation Complexes as Studied by Raman and FT-IR Spectroscopy. *J. Mol. Struct.* **1993**, *291*, 145-150.

(39) Nissinen, V. H.; Koshevoya, I. O.; Pakkanen, T. T. Crystalline Magnesium Chloride-Electron Donor Complexes: New Support Materials for Ziegler-Natta Catalysts. *Dalton Trans.* **2017**, *46*, 4452-4460.